ACS Catalysis

Research Article

pubs.acs.org/acscatalysis

Spectroelectrochemical Probing of the Strong Interaction between Platinum Nanoparticles and Graphitic Domains of Carbon

Jiwei Ma,[†] Aurélien Habrioux,[†] Cláudia Morais,[†] Adam Lewera,[‡] Walter Vogel,[§] Ysmael Verde-Gómez,[∥] Guadalupe Ramos-Sanchez,[⊥] Perla B. Balbuena,*[,⊥] and Nicolas Alonso-Vante*[,†]

[†]IC2MP, UMR-CNRS 7285, University of Poitiers, 4 rue Michel Brunet, 86022 Poitiers, France

[‡]Department of Chemistry, University of Warsaw, ul. Pasteura 1, 02-093 Warsaw, Poland

[§]Department of Chemistry, National Central University, No. 300 Jung-Da Rd., Chung-Li, Taoyuan 32001, Taiwan

[∥]Instituto Tecnológico de Cancún, Av. Kabah Km.3 s/n, CP 77500, Cancun, Q. Roo, Mexico

[⊥]Department of Chemical Engineering, Texas A&M University, College Station, Texas 77843, United States

Supporting Information

ABSTRACT: This study focuses on clarifying the strong interaction existing between extended graphitic domains of ordered carbonaceous materials such as multiwalled carbon nanotubes and platinum nanoparticles. This interaction results from the heterogeneous nucleation of platinum nanoparticles onto the carbon support. The metal clusters are chemically synthesized by using the carbonyl route. Two different carbon supports are used namely, homemade multiwalled carbon nanotubes, MWCNT-m, and classical Vulcan XC-72. Physicochemical properties of these materials are described by Raman spectroscopy, X-ray photoelectron spectroscopy (XPS), and X-ray diffraction (XRD). The effect of the strong interaction on the electronic properties of platinum nanoparticles is electrochemically probed by means of CO stripping experiments coupled with *in situ* Fourier transform infrared spectroscopy (FTIR). Density functional theory (DFT) is used to evaluate changes to the electronic structure of a platinum cluster interacting with a graphite substrate and their effects on CO adsorption on the cluster. Results are correlated with structural and electronic properties of platinum nanoparticles. The stability of Pt/carbon catalysts under electrochemical potential cycling is correlated with the properties of carbon substrates.

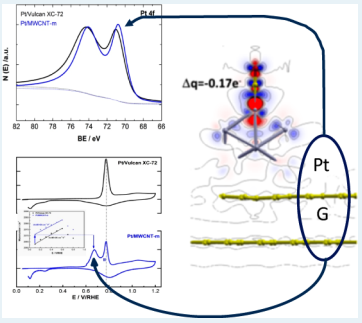

KEYWORDS: *platinum nanoparticles, graphitic carbon, XRD-XPS, in situ FTIR, DFT, (electro)catalysis*

1. INTRODUCTION

In catalysis and/or electrocatalysis, it is of interest to analyze the substrate used to transport the electrons to or from the reaction catalyst sites. Indeed, from a fundamental point of view, such an issue is relevant because nanoparticles can be influenced by the interaction between the nanoparticles and the support. The interaction between platinum nanoparticles and a substrate can be responsible for changes of their electronic properties. Strong interactions between platinum nanoparticles and oxides[1,2] or carbon-based materials[3−6] have already been demonstrated. Remarkably, it has been explained that Pt−C hybridization could be possible between platinum and carbonaceous materials possessing a high graphitization degree.[7] The strong interaction between carbon and platinum nanoparticles can be electrochemically probed by examining the desorption energy of an adsorbed model molecule such as carbon monoxide.[3,6] Changes in the electronic properties of the platinum valence band can be related to the modification of the Pt−CO bond strength[8] and as a result related to the CO desorption potential.[9,10] This is of importance since the synthesis of Pt/carbon catalysts able to oxidize adsorbed CO at low potentials is necessary for low temperature fuel cell technologies. CO is an oxidation intermediate of small organics and a parasitic product in the hydrogen reforming process. It has remarkably been demonstrated that a graphene-like carbon substrate exhibits an important influence on electrocatalytic oxidation of CO.[3,11] Additionally, the strong interaction between platinum and carbon-based materials is also of interest in order to enhance the stability of the catalyst.[12] An evident challenge in Proton Exchange Membrane Fuel cells (PEMFCs) is in fact the performance loss during extended cycling operation of the system. Indeed, the degradation of Pt-based catalysts, mainly due to the support oxidation, is known as one of the most serious reasons for the drop of the fuel cell performance. Vulcan XC-72 as a classical support for platinum nanoparticles oxidizes to CO_2 at $E \geq 0.97$ V vs RHE as revealed by differential electrochemical mass spectrometry (DEMS).[13] Platinum nanoparticles deposited onto carbon fibers as well as on single- or multiwalled carbon nanotubes have also been reported,[14] aiming at improving durability.

In this study, we focus on clarifying the nature of the strong interaction between platinum nanoparticles and carbonaceous

Received: February 26, 2013
Revised: July 9, 2013
Published: July 12, 2013

   dx.doi.org/10.1021/cs4003222 | ACS Catal. 2013, 3, 1940−1950

substrates with a high graphitization degree by means of XRD, XPS, cyclic voltammetry, DFT, and *in situ* FTIR analyses. The Pt/MWCNT-m system showed an increased CO-tolerance that can be correlated with the down-shift of the binding energy (BE) of Pt 4f electrons. This down-shift suggests an increased electron density on platinum, responsible for an enhancement of the back-donation of the platinum *d* orbital in the $2\pi^*$ antibonding orbital of CO, leading to a decrease in the Pt−CO bond strength. This observation is confirmed by coupling the CO stripping voltammetry and *in situ* FTIR. Furthermore, a pronounced enhancement of stability under potential cycling is obtained with Pt/MWCNT-m. This is due to the significant higher graphitization degree of the MWCNT-m substrate. To the best of our knowledge, this is the first time that the strong interaction between carbon-based substrates and platinum nanoparticles is studied by means of spectroscopic characterization methods, theoretical calculations, in order to probe the substrate induced modification of platinum nanoparticles. Furthermore, it is the first time that the effect of the long-range order of the carbon-based material on the magnitude of this interaction has been experimentally brought to light and theoretically explained.

2. EXPERIMENTAL SECTION

2.1. Synthesis of Multiwalled Carbon Nanotubes (MWCNT-m). The multiwalled carbon nanotubes (so designated MWCNT-m) used as support were synthesized at Instituto Tecnologico de Cancun using the chemical vapor deposition method (CVD). Ferrocene was dissolved in toluene. The solution was introduced in the liquid phase to the first reactor maintained at a low temperature. Then, the mixture was fed into a Vycor tube placed inside a tubular furnace at 900 °C with an argon atmosphere where the CVD reaction takes place. The MWCNTs were purified and activated by a reflux system using HNO_3 and washed several times with triple distilled water.

2.2. Synthesis of Pt onto MWCNT-m and Vulcan XC-72. Pt−carbonyl complexes were synthesized by using methanol as a solvent through the reaction of Pt under CO at around 50−55 °C for 24 h with constant stirring until the color of the solution turned to black green.[3,15] The molar ratio between Na^+/Pt^{IV} is fixed to 6. In this study, the structure of the carbonyl complex is suggested as the following structure due to the solution color: $[Pt(CO)_6]_n^{2-}$ with $n = 5$ or 6.[16] After synthesis of the Pt−carbonyl complex, the MWCNT-m was added to the carbonyl complex solution under an inert gas atmosphere for 12 h in order to obtain the catalyst with 20 wt % loading onto the substrates. The heterogeneous nucleation of Pt nanoparticles occurs on the carbon support. The powder was recovered after the solvent evaporation by rinsing with Milli-Q water (18.2 MΩ cm) to eliminate the impurities. The powder was recovered by filtration and then dried overnight. Vulcan XC-72 (preannealed at 400 °C for 4 h under N_2) was used to replace MWCNT-m for comparative study.

2.3. Physical and Electrochemical Characterization. *Raman Spectroscopy.* A Horiba Jobin Yvon Labram HR800UV Raman spectrometer provided with an Ar^+ laser (Melles Griot) as an illumination source equipped with a CCD cooled detector was used. The Raman instrument was coupled to an Olympus microscope with an analyzed region of a 100× microscope objective. The laser frequency used was the 514.5 nm line. The laser power at the sample was 0.04 mW. The spectra were recorded at 1 cm^{-1} resolution. Simulations were realized by using Fityk software.

X-Ray Diffraction (XRD) Analysis. X-ray patterns were obtained with a Guinier powder diffractometer (HUBER), set at the 45° transmission position. A Johansson type Ge monochromator produces a focused monochromatic Cu Kα-1 primary beam (λ = 0.15406 nm). The powder sample was slightly pressed and fixed between two 3 μm polyethylene foils and measured immediately under ambient conditions. A scan of the pure support materials: Vulcan XC-72 and MWCNT-m were used for the background correction. The background corrected patterns were subjected to the usual angular correction for absorption, polarization, and geometrical factors and plotted versus the reciprocal scattering length $b = 2 \sin \theta/\lambda$ (θ, Bragg angle; λ, wavelength). For the analysis of the X-ray data, we measured the integral line width (db) versus peak position (b_r) for the first five peaks (Williamson−Hall plot). The line profiles were fitted by the multipeak fitting package supplied by the IGOR software. The XRD single line profile analysis comes, however, to its limit of applicability for these extremely small particles. Mean crystallite sizes $\langle L \rangle$ can be evaluated, but the extraction of information about lattice defects (internal strains, stacking faults) is hampered by Bragg peak overlap of these cluster-like samples. Another approach used to extract data from XRD patterns is based on Debye function analysis (DFA).[17]

Transmission Electron Microscopy (TEM). The morphology of particles was examined with a TEM on a JEOL JEM-2001 equipped with a LaB_6 filament. The samples were characterized under an accelerating voltage of 200 kV and a resolution of *ca.* 0.19 nm. The corresponding particle-size distribution histograms were obtained, by measuring Feret's diameters of 200 particles for each sample.

X-Ray Photoelectron Spectroscopy (XPS). X-ray photoelectron spectroscopy measurements were performed with a Microlab 350 spectrometer using Al Kα nonmonochromated radiation (1486.6 eV, 300 W) as the exciting source. The pressure during analysis was 5.0×10^{-9} Pa. The BE of the target elements (Pt 4f, O 1s, and C 1s) was determined at a pass energy of 40 eV, with a resolution of 0.83 eV. To avoid charging, samples were immobilized using conducting glue. XPS spectra were fitted using CASA XPS software. Hybrid Doniach Sunjic/Gaussian−Lorentzian (sum) line-shape was used, and the C1s were fitted with three singlets (for different C-containing components) and Pt 4f spectra with one Pt 4f doublet. The same line shape parameter has been used for both samples. BE scales were calibrated with Au, Ag, and Cu standards, as recommended by the National Institute of Standards and Technology (NIST).

Electrochemistry. The catalytic ink was prepared as follows: a mixture containing 10 mg of catalytic powder, 250 μL of Nafion solution (5 wt % in water/aliphatic alcohol solution, Sigma-Aldrich), and 1250 μL of Milli-Q water (18.2 MΩ cm) was sonicated for 30 min, and then an aliquot of 3 μL of the mixture was dropped onto the glassy carbon disk (GC) electrode (surface area of 0.071 cm^2) and dried in a stream of inert gas (argon) at room temperature for 30 min.

The electrochemical measurements were carried out at 25 °C by using a potentiostat (Autolab PGSTAT 30) in a thermostatted three-electrode cell. The electrolyte was prepared by using concentrated H_2SO_4 (Suprapur, Merck) and Milli-Q water (18.2 MΩ cm). A plate of glassy carbon (GC) and a reversible hydrogen electrode (RHE) were used as counter and

reference electrodes, respectively. The RHE was connected to the working electrode through a Luggin capillary. The catalysts' performances were evaluated by cyclic voltammetry (CV) at 25 °C in a N_2-saturated 0.5 M H_2SO_4 solution from 0.05 to 1.2 V vs RHE at a scan rate of 50 mV s^{-1}. The electrochemical active surface area (ESA) was calculated by measuring the charge obtained in the H_{upd} adsorption/desorption area after double-layer correction and assuming a value of 210 μC cm^{-2} for the adsorption of a hydrogen monolayer.[18] The electrochemical stability study of Pt/MWCNT-m and Pt/Vulcan XC-72 electrocatalysts was evaluated by the accelerated durability tests (ADT) in the potential range of 0.05−1.2 V vs RHE during 3000 cycles with a scan rate of 50 mV s^{-1}. For CO-stripping experiments, CO was bubbled into the electrolyte (0.5 M H_2SO_4) for 10 min, while the working electrode is biased at 0.1 V vs RHE. Then, dissolved CO was removed by bubbling nitrogen gas for 20 min. Two successive cyclic voltammograms were recorded from 0.05 to 1.2 V vs RHE with a scan rate of 5 mV s^{-1}.

In Situ Infrared Reflection−Absorption Spectroscopy Measurements. The Fourier transform infrared (FTIR) reflection−absorption technique combined with CV electrochemical measurements was employed for an *in situ* monitoring of the CO oxidation to therefore obtain microscopic-level information regarding the interaction between the catalyst and the probe chemisorbed molecule. The *in situ* FTIR experiments were carried out under external reflection conditions on a Bruker IFS66v spectrometer modified for beam reflectance at a 65° incident angle and equipped with a liquid N_2-cooled MCT detector. In order to avoid IR bands from atmospheric CO_2 and H_2O, all of the system is maintained under a vacuum. All of the experiments were performed in a three-electrode spectroelectrochemical cell fitted with a CaF_2 window on the bottom. The reference electrode was a reversible hydrogen electrode (RHE), and a platinum wire was used as the counter electrode. The working electrode consisted of a polycrystalline Au disc connected to a glass shaft. The deposition of platinum samples on the surface gold disc, previously polished to a mirror finish, was performed by pipetting 5 μL of a catalyst ink containing 6.7 mg mL^{-1} of catalyst.

The adsorption of CO was conducted by bubbling CO for 5 min under potential control at 0.1 V vs RHE. The electrolyte was then purged with N_2 for 25 min, maintaining the polarization of 0.1 V vs RHE. Thereafter, the electrode was pressed to the CaF_2 IR window, and a series of spectra were acquired at subsequently applied electrode potentials in the range of 0.1−1.0 V vs RHE at 50 mV intervals at a scan rate of 1 mV s^{-1}. For each spectrum, 512 interferograms were collected at a resolution of 8 cm^{-1}. IR spectra were calculated for each potential value as changes in the reflectivity (R) relative to a reference single-beam spectrum (R_{ref}) as follows: $(\Delta R/R)_i = (R_i - R_{ref})/R_{ref}$. Positive and negative going bands represent, respectively, the decrease and increase of species.

2.4. DFT Analyses. In order to investigate the electronic properties of the system, we performed a DFT analysis of the interaction between a graphite model and adsorbed Pt clusters. The graphite model consists of three layers of graphene; each graphene layer is a 5 × 5 structure, in total 150 C atoms, 50 in each layer. A Pt_{13} cluster was allowed to interact with graphite. This cluster size is intended to capture changes in electronic structure due to the presence of the substrate, especially for Pt atoms at the interface and its vicinity. The Pt_{13} cluster used for the simulation has icosahedral symmetry with one of the three-atom facets allowed to interact with graphite. In our earlier work,[19] we reported the energetic differences between the Pt_{13} cluster in icosahedral and cube-octahedral geometries. The cube-octahedral cluster is slightly more stable than the icosahedral; however the energetic difference is only 0.08 eV using the PBE exchange-correlation functional. This difference is similar to that reported with the PW-91 functional.[20] We note that ref 20 also reports several other structures that are more stable than the icosahedral and cube-octahedral geometries for Pt_{13} in a vacuum. In this work, regarding the adsorption of the cluster on graphite, a full search of a global minimum was not conducted, but both structures (icosahedral and cube-octahedral) were tested and found to be local minima. It was found[19] that stronger adsorption energy occurs when the Pt atoms are on top and bridge positions of the graphite substrate, compared to adsorption on the center of the graphite hexagons; in this sense, the three-atom facet of the icosahedral seems perfect to interact either in top or bridge positions on the graphite surface. We demonstrated that the adsorption of the icosahedral cluster is preferred over the cube-octahedral cluster owed to a best match of this three-atom facet with graphite.[19] Other calculations done with a series of cluster sizes from 1 to 38 atoms have been reported recently including charge transfer characteristics and modifications of the DOS for both Pt cluster and graphite after adsorption;[19] the charge distribution of Pt_{38} is included as Supporting Information, Figure S1. The Pt_{13} cluster was selected because the observed trends are similar to those shown by larger clusters, and it has served as a model of recent theoretical studies.[21,22] The calculations were performed with the Vienna ab initio Simulation Package (VASP), allowing spin-polarization and using the projector augmented wave (PAW) method. The electron exchange correlation was treated within the spin polarized general gradient approximation and the Perdew−Becke−Ernzerhoff (PBE) functional. The DFT-D2[23,24] approach implemented in VASP is used to account for the vdW interactions; the inclusion of vdW forces is mandatory for the correct representation of the interlayer distance in graphite.[19] This approach, despite being semiempirical, has been used successfully in a series of results reported recently not only in layered compounds but also in metallic systems: it has been used in Cu−graphene systems yielding graphene−metal distances within the 0.2% of the experimental value,[25] in the interaction of Au clusters with pyridine rings where it not only qualitatively but also quantitatively represents the experimental forces in the system,[26] and in the interaction of polar molecules with metallic Pt(111) correctly described using the DFT-D2 approach.[27] In a recent report, we have discussed extensively the effect of the DFT-D2 approach to the geometries and electronic structure of Pt clusters supported on graphite.[19] In this paper, the inclusion of the semiempirical approach for vdW interactions aims to a better description of the graphite−metal and cluster−CO interaction. The cutoff energy for the plane-wave basis expansion was chosen to be 400 eV. A quasi-Newton algorithm is used to relax ions into their instantaneous ground state. The ions were allowed to relax, but the cell size and shape were kept constant. The method of Methfessel−Paxton[28] of first order was used to represent partial occupancies and a conjugate gradient algorithm for electronic minimization. The criteria for ionic and electronic convergence were set to 10^{-4} and 10^{-5} eV, respectively. After the graphite−Pt cluster optimization was carried out, a CO molecule was allowed to interact with the cluster, and the complex was reoptimized.

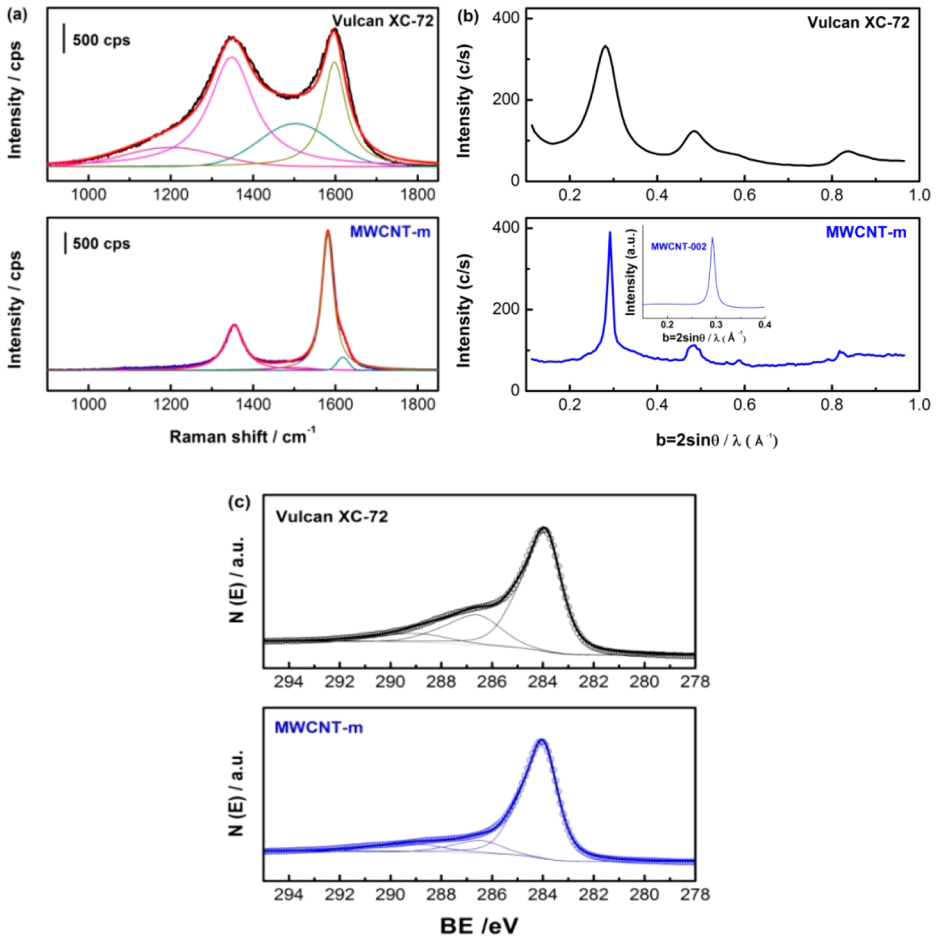

Figure 1. (a) Raman spectra, (b) XRD patterns, and (c) C 1s XPS of Vulcan XC-72 and MWCNT-m.

3. RESULTS AND DISCUSSIONS

3.1. Physicochemical Characterization of Pure Carbon Substrates (MWCNT-m, Vulcan XC-72). Raman spectra recorded in the spectral region of 1000−1800 cm^{-1} with Vulcan XC-72 and MWCNT-m samples are presented in Figure 1a. Several overlapping bands can be observed. The D and D′ bands are defect-induced ones. By reason of the amazing intensity of the band centered at *ca.* 1500 cm^{-1}, it is evident that the graphitic structures of Vulcan XC-72 possess a high degree of interstitial disorder along the *c* axis between the crystallite planes.[29] Additionally, this carbonaceous material contains more sp^3-rich phases than MWCNT-m since the intensity of its 1200 cm^{-1} band is huge. Simulations of the two spectra were performed by using Lorentzian line shapes for D and G bands,[29−31] and Gaussian ones for the D′ band[30−32] as well as for bands centered at *ca.* 1200 cm^{-1}[29,33] and 1500 cm^{-1}.[29] For the fitting, the positions of D and G bands were set by taking into account the positions of 2D (*ca.* 2700 cm^{-1}) and D + G (*ca.* 2940 cm^{-1}) bands. The results of the best fits provided several parameters which are summarized in Table 1. The upward shift observed for the G-band of Vulcan XC-72, located at 1598 cm^{-1}, probably results from the higher degree of disorder of the corresponding sample. It is well-known that the G band of disordered materials is shifted to higher Raman wave numbers than the G band of ordered ones.[34] This shift is responsible for a total overlapping of G and D′ bands. As a result, the observed bands include both G and D′ ones. The magnitude of the shift is directly related to the percentage of contribution of D′.[35] The disordered character of the Vulcan XC-72 sample is in fair agreement with the observed D and G line widths of this sample. The decrease in both band widths is evidence for the increase of the ordering degree. All these conclusions are concomitant with the information obtained by XRD patterns of MWCNT-m and Vulcan XC-72 materials shown in Figure 1b. The morphology of the two carbon-based supports is very different, which is also reflected in their XRD patterns. The major carbon-002 Bragg peak profile (peak position and integral width) gives the mean wall thickness of 5.7 nm for the MWCNT-m, with 17 intercalated walls on average forming the nanotubes. In contrast, the broad carbon-002 peak of porous Vulcan XC-72 relates an average stack size around 1 nm, formed by three highly disordered graphitic layers. From the Raman spectra, it is also possible to quantify

Table 1. Raman Parameters Obtained from Spectra Fitting[a]

	Vulcan XC-72	MWCNT-m
υ_D (cm^{-1})	1350	1354
$\omega_{1/2D}$ (cm^{-1})	131	56
υ_G (cm^{-1})	1598	1582
$\omega_{1/2G}$ (cm^{-1})	66	34
I_D/I_G	2.1	0.5
L_a (nm)	8	31.5

[a] υ_D and υ_G respectively correspond to D and G band positions. $\omega_{1/2D}$ and $\omega_{1/2G}$ respectively correspond to the full width at half maximum of D and G bands. L_a represents the in-plane crystallite size determined from eq 1.

dx.doi.org/10.1021/cs4003222 | ACS Catal. 2013, 3, 1940−1950

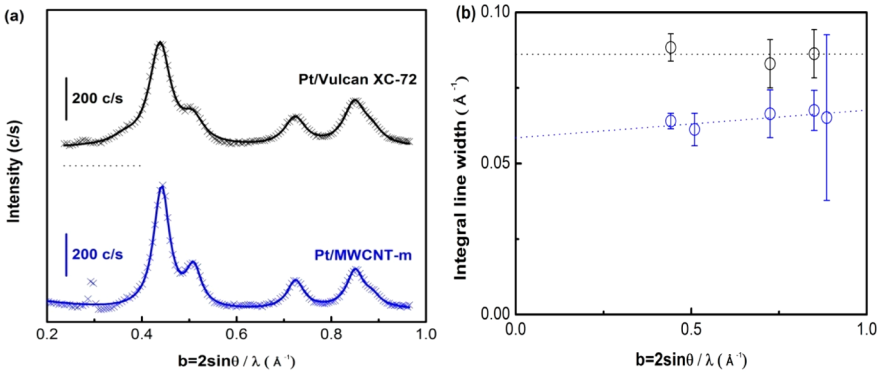

Figure 2. (a) XRD patterns of Pt/Vulcan XC-72 and Pt/MWCNT-m catalysts. (b) Williamson−Hall plots of the integral width extracted from the fitting.

the degree of graphitization of a carbonaceous material by evaluating the D to G band intensity ratio (I_D/I_G) ratio. This ratio is commonly used to quantify the amount of defects in the carbonaceous materials as well as their in-plane crystallite size (L_a). One of the relations describing the evolution of L_a with the integrated intensity ratio of G to D bands is the following one:[36]

$$L_a\ (\mathrm{nm}) = 2.4 \times 10^{-10} \lambda_{laser}{}^4 \frac{I_G}{I_D} \quad (1)$$

where, λ_{laser} is the laser wavelength in nm.

From the L_a values, it can be deduced that Vulcan XC-72 has a lower in-plane crystallite size than MWCNT-m and does not possess extended graphitic domains. The width of the D band observed with the Vulcan XC-72 sample furthermore reflects a broad distribution of in-plane crystallite size. XPS spectra of the C1s region of MWCNT-m and Vulcan XC-72 have been recorded and are shown in Figure 1c. The C1s region has been fitted with three components: at *ca.* 284 eV (elemental carbon), at *ca.* 286.5 eV (organic compounds from conducting glue, BE determined in a separate experiment), and at 289.5 eV (some species containing C−O bond). In conclusion, both substrates contain a similar amount of oxygenated chemical groups grafted onto their surface. We note that the substrate model used for the DFT calculations discussed in the next two sections resembles more the structure of a multilayer nanotube (NT) with a high degree of symmetry than the highly disordered Vulcan XC-72 that does not possess an ordered graphitic structure.

3.2. Physicochemical Characterization of Pt/Carbon (Carbon = MWCNT-m, Vulcan XC-72) Catalysts. Figure 2a shows the XRD patterns of platinum corrected by the carbon background produced by the MWCNT-m and Vulcan XC-72, respectively. The patterns clearly exhibit the FCC symmetry with the first five Bragg peaks. These peaks have been fitted by overlapping symmetrical Lorentzian functions as shown by the solid lines in the figure. The integral line widths δb_{hkl} of the fit are shown in a Williamson−Hall graph in Figure 2b versus their peak positions b_{hkl} in a b scale. Linear extrapolation of this graph to $b = 0$ (see dashed line in Figure 2b) leads to the mean crystallite size $\langle L \rangle$ = 1.64 nm. Assuming a particle shape close to be spherical, this would correlate to a mean particle diameter $\langle D \rangle = 3/2$ and $\langle L \rangle$ = 2.46 nm. For the Pt/MWCNT-m catalyst, the width of five lines does not deviate from a linear slope within their limits of error, which indicates a relatively ordered nanolattice. The nonzero slope can be interpreted by some degree of internal strains, but a quantitative analysis would be ambiguous. For the Pt/Vulcan XC-72 catalyst, only the three clearly visible Pt peaks, 111, 220, and 311, were shown in the Williamson−Hall plot due to severe overlap, limiting the accuracy of the weak Pt-200 and Pt-222 peaks. The crystallite size of the Vulcan XC-72 supported Pt catalyst is even smaller, with $\langle L \rangle$ = 1.20 nm or $\langle D \rangle$ = 1.80 nm.

The higher graphitization degree of MWCNT-m, as revealed by Raman experiments, is probably responsible for slightly decreasing the number of nucleation sites that favor the formation of bigger platinum particles.[37] This could be due to a higher effective surface energy responsible for increasing the free energy barrier. This does not favor the heterogeneous nucleation of particles.

TEM micrographs of Pt/Vulcan XC-72 and Pt/MWCNT-m are shown in Figure 3a and c. The corresponding particle-size distribution histograms are presented in the Figure 3b and d. We observed that the platinum nanoparticles are uniformly dispersed on the carbon substrate. It can be clearly stated that the size distributions of both catalysts clearly overlap. The mean particle sizes for Pt/Vulcan XC-72 and Pt/MWCNT are

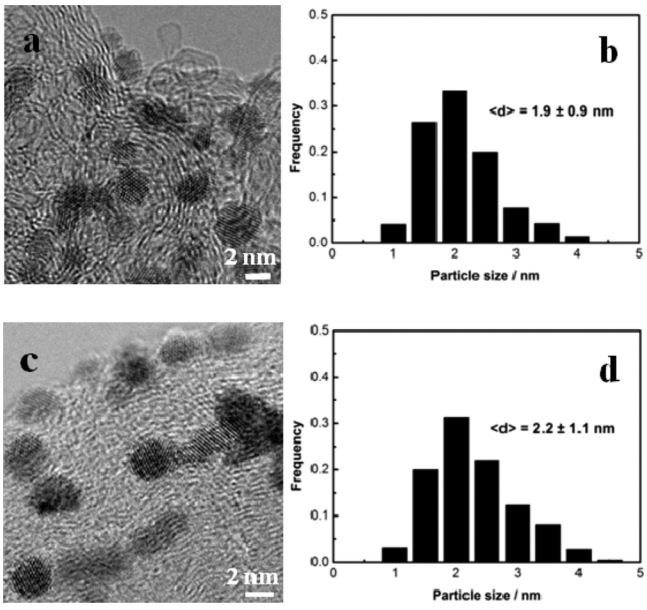

Figure 3. TEM images and corresponding size distribution histograms for (a) and (b) Pt/Vulcan XC-72 and (c and d) Pt/MWCNT-m catalysts.

dx.doi.org/10.1021/cs4003222 | *ACS Catal.* 2013, 3, 1940−1950

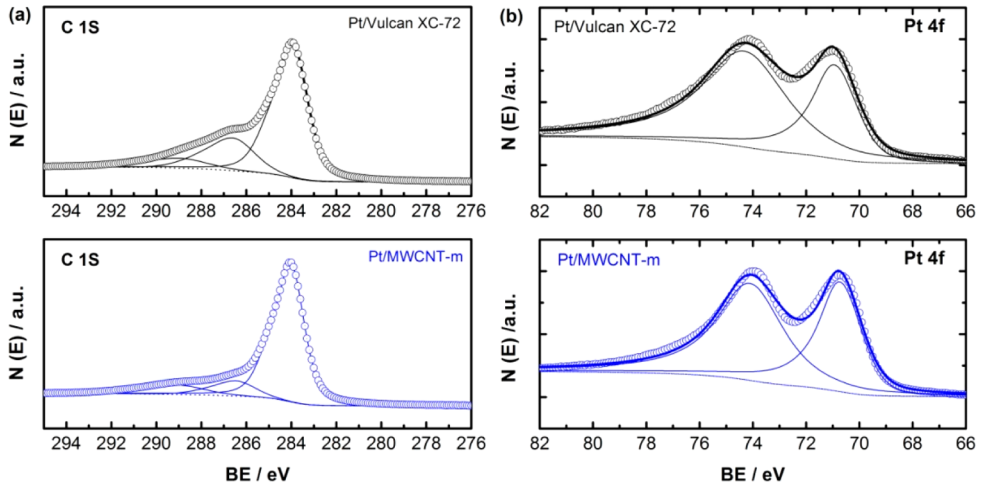

Figure 4. XPS spectra of (a) C 1S and (b) Pt 4f regions of Pt/Vulcan XC-72 and Pt/MWCNT-m catalysts.

respectively 1.9 and 2.2 nm. The difference in the mean particle size is due to a slight broadening of the size distribution for Pt/MWCNT sample.

In order to characterize charge transfers occurring between carbon and platinum, X-ray photoelectron spectroscopy (XPS) experiments were carried out, Figure 4. The comparison of C1s signals between pure substrates and Pt-containing systems is presented in Table 2. Pt 4f signals have been fitted with one doublet. Pt $4f_{7/2}$ peak parameters are presented in the Table 2. It can be seen that, in general, the C1s signal is slightly broader and downshifted in the case of Vulcan XC-72 as compared to MWCNT-m. It is interesting to note that Pt deposition causes a BE shift of the C1s signal by *ca.* 30−40 meV toward lower values, which suggests a partial charge transfer from Pt to C, more pronounced in the case of Pt/Vulcan XC-72. When compared with the Pt 4f signal (see Table 2), it becomes clear that the charge transfer from Pt to C is more evident in the case of Pt/Vulcan XC-72, thus leaving the Pt/MWCNT-m system with higher electron density on Pt as compared to Pt/Vulcan XC-72. Particularly, the Pt/MWCNT-m system compared to Pt/Vulcan XC-72 shows a *ca.* 210 meV downshift of the BE of Pt 4f electrons. Though the resolution is 0.83 eV, the shift observed between the two signals is significant. It should actually be pointed out that the resolution in general is the resolving power of any instrument. It is not correlated to the accuracy of the energy scale. The data points were collected each 50 meV, so each signal (width *ca.* 5 eV) is composed of 100 data points. It is arguable whether better accuracy than 50 meV can be achieved when all the data points are fitted with a synthetic line shape, but a 210 meV BE shift is easily observed.

From the DFT calculations, analyses of Bader charges[38] indicate that there are 0.15 electrons of total charge transfer from a Pt cluster of 13 atoms to graphite. This charge transfer was calculated as the difference of the sum of the Bader charges of all cluster atoms before and after the interaction with the carbon substrate. Despite the small charge transfer value,

Table 2. Positions and Full Widths at Half Maximum (FWHM) of C1s Peak for Pure Carbon Substrates (MWCNT-m, Vulcan XC-72) and of C1s and Pt4f Peaks for Carbon Substrate-Supported Platinum

	C1s BE/eV	C1s fwhm	$Pt4f_{7/2}$ BE/eV	$Pt4f_{7/2}$ fwhm
MWCNT-m	284.03	1.41		
Pt/MWCNT-m	284.00	1.46	70.75	1.89
Vulcan XC-72	283.94	1.55		
Pt/Vulcan XC-72	283.90	1.56	70.96	1.99

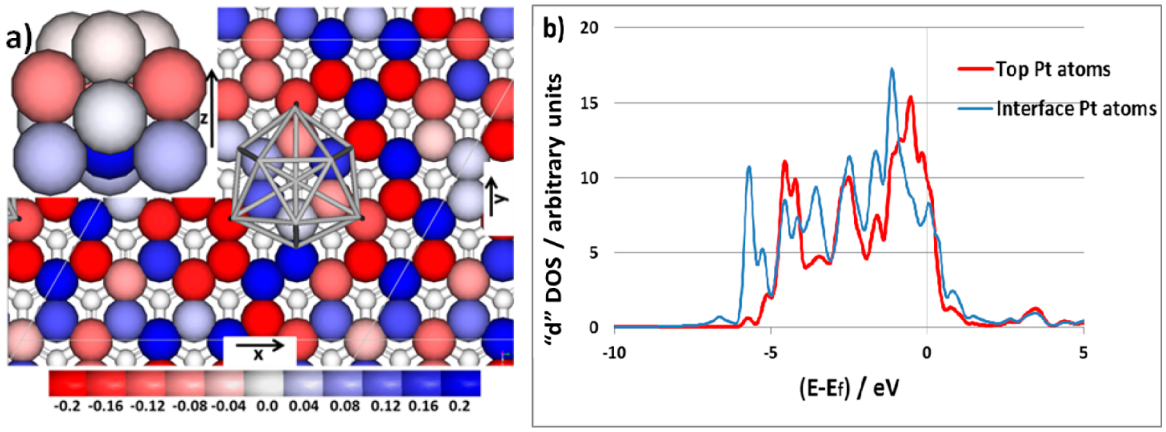

Figure 5. (a) Bader charge difference (Bader charge after, minus Bader charge before adsorption) of graphite and Pt_{13} cluster (inset). Scale is shown at the bottom (unit: e). (b) Local density of states (d states) of the platinum cluster atoms at the interface and atoms in the top of the cluster shown separately. The horizontal axis is the energy difference ($E - E_f$) with respect to the Fermi level (E_f), that is therefore located at 0 eV.

dx.doi.org/10.1021/cs4003222 | *ACS Catal.* 2013, 3, 1940−1950

individual Bader charge values are more affected, not only those atoms at the cluster−graphite interface but all of them. Figure 5a depicts the changes of individual Bader charge values after adsorption for the interacting Pt/graphite system. We evaluate the difference of the Bader charges after, minus the Bader charges before adsorption; using this definition, a positive value means charge deficiency and a negative value means charge excess. It is found that near the cluster/substrate interface the carbon atoms have an excess charge (more negative values), whereas the Pt atoms have a deficiency of electrons (thus, becoming positively charged). An interesting aspect which may have consequences in catalysis is the polarization of the metal cluster, with the top Pt atoms bearing partial negative charge and those at the interface, partial positive charge. We note that the model used in the simulations represents a perfect graphitic structure in which there is a moderately low charge transfer. This scheme may differ from other carbon structures; for example, it has been reported that defective graphene may accept higher charge transfer from Pt clusters (0.24 e),[22] and there is no accumulation of charge in Pt top atoms. However it should be noted that Pt_{13} clusters interacting with defective and non-defective substrates adopt very different geometries after adsorption.

3.3. Electrochemical Probing Substrate Induced Electron Density on Platinum. *3.3.1. Voltammetric Experiments.* CO-stripping voltammograms recorded with different Pt/carbon (carbon = Vulcan XC-72 or MWCNT-m) catalysts synthesized by using the carbonyl route are shown in Figure 6.

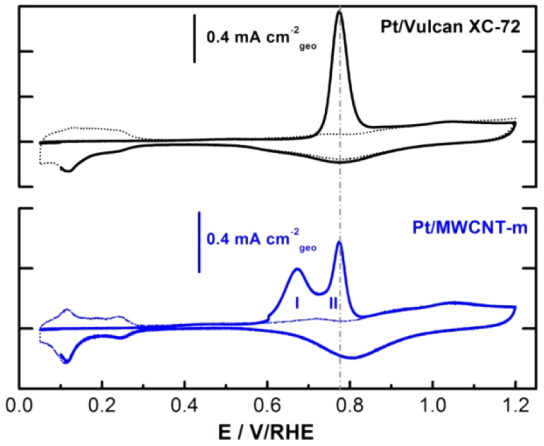

Figure 6. Comparison of CO stripping curves in 0.5 M H_2SO_4 from 0.05 to 1.2 V/RHE with a scan rate of 5 mV s^{-1} for Pt/Vulcan XC-72 and Pt/MWCNT-m catalysts.

The main CO oxidation potential region (0.60 V vs RHE < E < 0.90 V vs RHE) is composed of two oxidation peaks. They are respectively located at *ca.* 0.68 V vs RHE (peak I) and *ca.* 0.76 V vs RHE (peak II). TEM experiments carried out with both samples (Figure 3a and c) show that no significant differences have been observed between Pt/MWCNT-m and Pt/Vulcan XC-72 samples in what concerns the agglomeration degree of Pt nanoparticles. Additionally, TEM experiments were also carried out using the catalytic inks. Results indicate that the adding of Nafion (which acts as a surfactant molecule) allows for an increasing dispersion of particles.[39] In conclusion, the agglomeration effect which could be responsible for peak I[40−43] can be ruled out as a source of peak multiplicity observed during CO-stripping experiments performed with the Pt/MWCNT-m catalyst. It is furthermore difficult to consider a size effect to explain the obtained results. The observed slight difference in the size distributions, cf. Figure 3b and d, that concerns *ca.* 10−15% of the particles cannot explain the magnitude of the first peak observed during the CO stripping experiment on the MWCNT-supported platinum nanoparticle catalyst. By taking into account the results obtained from Raman experiments, it can be stated that the first and second peaks can be respectively attributed to the CO oxidation from platinum sites interacting with graphitized and disordered carbon structures.[3] The occurrence of the double peak and their relative magnitudes are just related to the ratio of disordered to ordered domains of the carbonaceous materials. As a consequence, the appearance of the double peak can be clearly related to different electron densities on platinum as revealed by the observed down-shift BE of Pt 4f electrons, cf. Figure 4. This down-shift explains the increased catalytic oxidation of CO on Pt/MWCNT-m.

The adsorption phenomenon of CO at the platinum surface is accompanied by the back-donation of the platinum d orbital in the $2\pi^*$ antibonding orbital of CO (Blyholder−Bagus back-donation mechanism).[44,45] This process is more pronounced on a surface with higher electron density, as in the case of Pt/MWCNT-m in comparison to Pt/Vulcan XC-72. The increase of the electron density on platinum for the Pt/MWCNT-m sample compared to that of Pt/Vulcan XC-72 clearly results from the heterogeneous nucleation of platinum nanoparticles on a carbonaceous material possessing a high graphitization degree (see L_a values in Table 1). Certainly, the extended π systems are responsible for the anchoring of particles[7] strongly modifying d-band properties of platinum as observed in Figure 5b, where the density of states (DOS) of the platinum atoms changes because of the strong interaction as a result of Pt−C hybridization. In ref 19, we showed the states resulting from the interaction of graphite with the clusters. Moreover, the "d" DOS of the atoms with higher electronic density (top atoms in the cluster) has more states near the Fermi level (E_f) in comparison to those of the interface Pt atoms having a deficit of charge; the "d" bandwidth of the top Pt atoms is −2.18 eV and that of interface atoms is −2.58 eV. Figure S1 (Supporting Information) illustrates that similar changes occurring in Pt_{13} when interacting with graphite also are found in a 1 nm cluster (Pt_{38}), where electron sharing and depletion is observed at the interface and accumulation in all other areas even at the top of the cluster. As a consequence of the higher electronic density, the adsorption energy of CO is supposed to be preferred in the top Pt atoms compared to that occurring on the interface atoms. However, after interaction with the CO molecule, the geometry of the cluster is modified in order to obtain the lowest energy structure. As a result of the modification of the cluster structure, after optimization, the CO molecule always adsorbs in sites with an excess of electrons. If the molecule is allowed to interact with a positively charged site, the cluster structure reconstructs and the CO migrates to a site with higher electronic charge.

On the basis of previously presented XRD measurements, it was shown that the nonzero slope depicted in the Williamson−Hall plot for the Pt/MWCNT-m sample could be associated to some degree with the internal strains in the sample. These strains are probably the result of the strong Pt−C interaction[8] and are related to a crystal lattice contraction effect (isostatic strain). The contraction effect can be associated with an increase of d orbitals overlapping resulting from an enhance-

dx.doi.org/10.1021/cs4003222 | ACS Catal. 2013, 3, 1940−1950

ment of $d-d$ interactions between platinum atoms. By taking into account the d-band dispersion theory developed by Dimakis et al.,[46,47] the previous observations are in agreement with the increase of back-donation of the platinum d orbital to the $2\pi^*$ antibonding orbital of CO. The back-donation of charge from platinum to the CO $2\pi^*$ antibonding orbital is represented in Figure 7, where depletion of the charge is

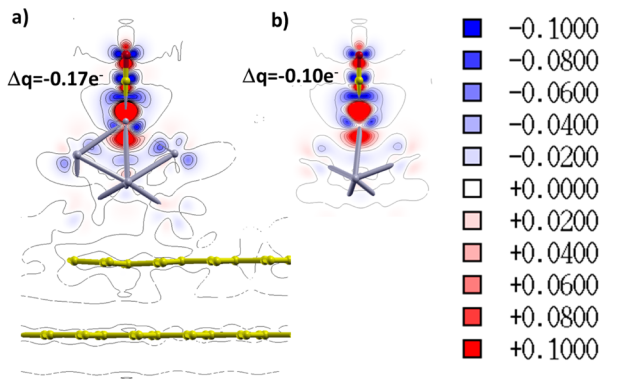

Figure 7. Charge accumulation (blue) and depletion (red) calculated as the difference of electronic density between the graphite−Pt−CO system and the electronic density of isolated graphite−Pt and CO (negative values indicate electronic density excess, and positive values denote electronic density deficit). (a) Cluster with graphitic substrate. (b) Free cluster, the value in the figure represents the charge difference in the C atom after adsorption. The scale of charge depletion/accumulation is depicted at right.

observed in the Pt atom directly interacting with CO, whereas accumulation of charge is found in the C and O atoms. This donation is made by the nodal plane instead of by the Pt−C−O axis, which clearly reflects the back-donation scheme. The amount of charge transferred is inversely proportional to the CO adsorption energy. The adsorption energies of CO in the same cluster and the same position with and without graphite are −2.60 and −2.85 eV, respectively, i.e., 0.25 eV weaker as a result of the interaction of the Pt cluster with a highly graphitized substrate. The back-donations to the $2\pi^*$ antibonding orbital can be related to the quantity of charge lost by platinum and the charge accepted by the carbon atom in the carbon monoxide molecule; in the free and supported cluster the charge accepted by the carbon atom is 0.1 and 0.17e, respectively, which confirms that sites with higher charge density enhance CO oxidation. The enhancement of the charge density is only possible because of the interaction with the high graphitized support. As observed in Figure 7, graphite contributes with a small but significant charge transfer that does not exist in the free cluster. Therefore, the substrate plays an important role during CO oxidation by facilitating charge transfer to the CO molecule. The results discussed for Pt_{13} represent an ideal case for the adsorption of CO in a small cluster. Since in this case there is cluster reconstruction after adsorption, the different CO adsorption strength and charge transfer may be attributed to the change of geometry. In order to investigate this point, we adsorbed CO on a larger cluster (Pt_{19}) in which only slight changes in geometry are found after adsorption, and we performed a similar analysis as in Pt_{13}, as shown in Figure S2 (Supporting Information). The cluster follows the same trends in adsorption strength and charge transfer. The CO adsorption energies in substrate-free and supported clusters are −2.32 and −1.98 eV, respectively, and the charges transferred to C by back-donation of Pt are 0.1 and 0.13e, respectively.

From the amount of charge associated with the H_{upd} region for each sample from the voltammetric cycle noted 0 in Figure 8a, it can be stated that the ESA of Pt/MWCNT-m (1.29 cm^2) is lower than the ESA of the Pt/Vulcan XC-72 (1.68 cm^2) sample. The ESA value for Pt/MWCNT-m sample is due to a low mass metal loading as confirmed by TGA experiments, Figure S3 (Supporting Information). It is the 16 wt % Pt/MWCNT-m sample that leads to a value of ESA or Pt mass loading of *ca.* 40 m^2/g_{Pt}, whereas 19 wt % for the Pt/Vulcan XC-72 sample leads to a value of ESA or Pt mass loading of *ca.* 44 m^2/g_{Pt}. However, this fact cannot be an argument to explain the observed differences of the CO stripping experiments. Indeed, an increase of the mass metal loading is not responsible for a negative shift of the main CO oxidation peak or for a positive one, as shown in Figure S4 (Supporting Information). Additionally, after 3000 voltammetric cycles in the 0.05−1.2 V vs RHE potential range, the Pt/MWCNT-m catalyst retains *ca.* 70% of its initial ESA with a value of *ca.* 0.90 cm^{-2}. Under the same cycling conditions, the Pt/Vulcan XC-72 catalyst only retains *ca.* 25% of its initial ESA with a value of *ca.* 0.42 cm^{-2}, as shown in Figure 8b. A size effect cannot explain the obtained results, as size distributions of the two samples clearly overlap (Figure3a and b). Moreover, it is well known that particles supported on carbon-based materials possessing a high

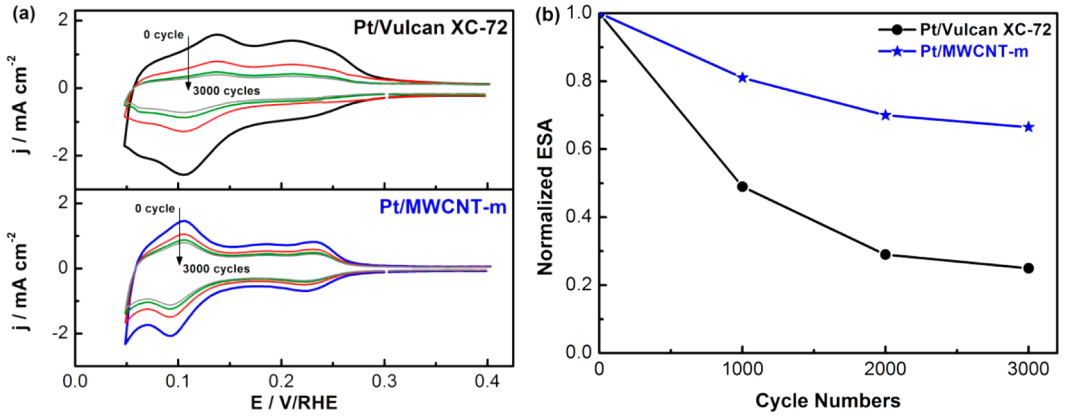

Figure 8. (a) Cyclic voltammogramms to determine the ESA and (b) normalized ESA loss under potential cycling from 0.05 to 1.2 V vs RHE in N_2-saturated 0.5 M H_2SO_4 with a 50 mV s^{-1} scan rate at 25 °C for Pt/Vulcan XC-72 and Pt/MWCNT-m catalysts.

dx.doi.org/10.1021/cs4003222 | *ACS Catal.* 2013, 3, 1940−1950

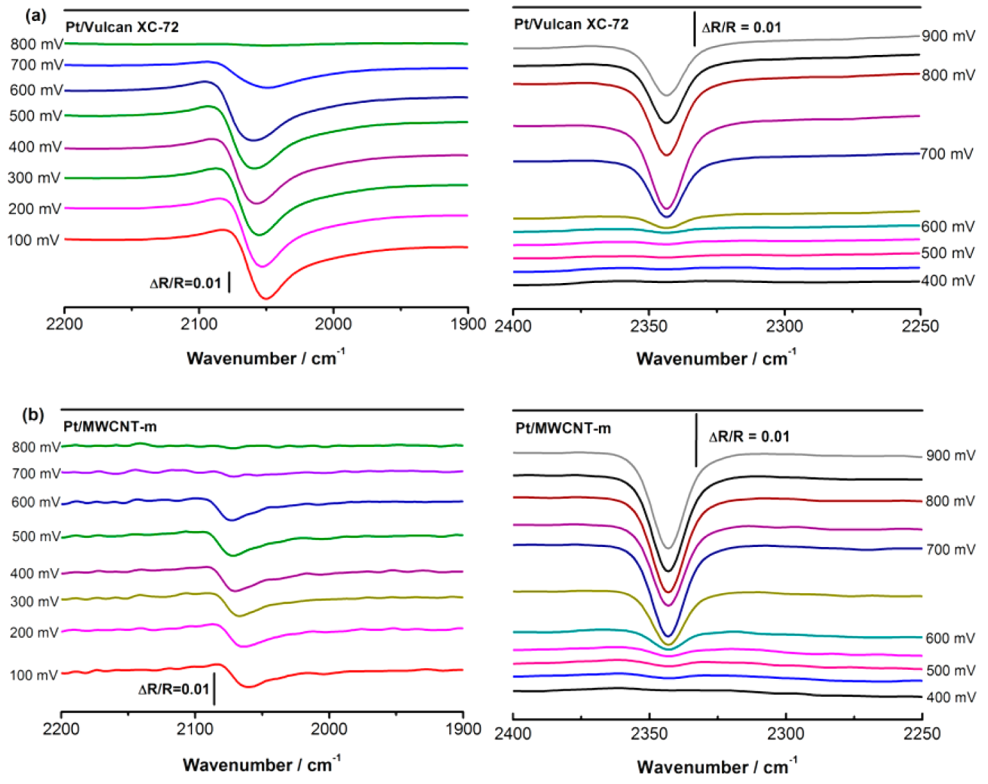

Figure 9. *In situ* FTIR spectra obtained for (a) Pt/Vulcan XC-72 and (b) Pt/MWCNT-m catalysts during CO stripping in 0.5 M H_2SO_4 electrolyte. The sample potentials are indicated. For the CO_L region (left figure), the reference potential was taken at 1 V/RHE corresponding to a CO-free electrolyte. The CO_2 region (right figure, band at 2342 cm^{-1}) was calculated with the reference spectrum taken at 0.1 V/RHE where CO_2 is not yet formed.

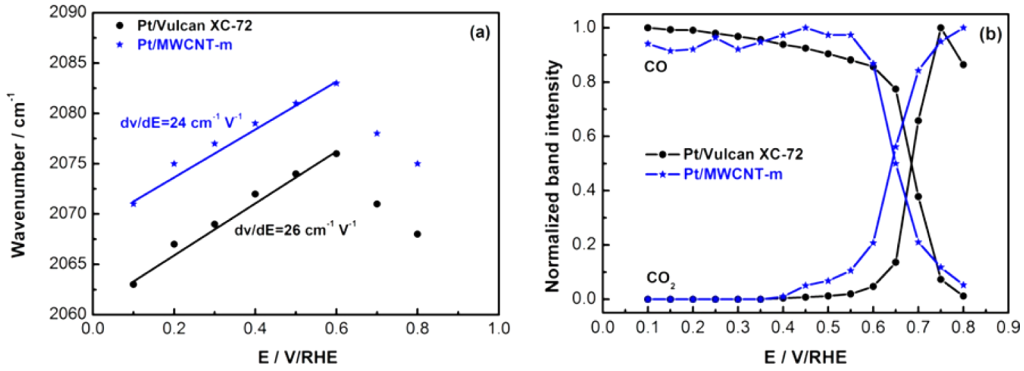

Figure 10. (a) Potential dependence of the C−O stretching wavenumber for on-top CO_L for Pt/Vulcan XC-72 and Pt/MWCNT-m. (b) Potential dependence of the normalized CO_L and CO_2 band intensities calculated from FTIR spectra.

graphitization degree are highly subjected to agglomeration.[37] By taking into account the results obtained from Raman experiments, the MWCNT-m sample possesses a higher graphitization degree than Vulcan XC-72. As a consequence, if this effect was the main contributor to ESA loss, this latter would be larger for the Pt/MWCNT-m sample than for the Pt/Vulcan XC-72 catalyst. Thereafter, the strong interaction between platinum nanoparticles and the extended graphitic domains is responsible for increasing the stability of the Pt/MWCNT-m catalyst under potential cycling. This strong interaction probably limits the agglomeration of platinum nanoparticles under potential cycling. Furthermore, it is well-known that highly ordered graphitic carbons such as MWCNT-m are less susceptible to the corrosion phenomenon than disordered carbonaceous materials such as Vulcan XC-72.[48] The high corrosion resistance of MWCNT-m results in the high stability of the Pt/MWCNT-m catalyst. Indeed, the increased graphitized degree leads to an increased strength of π sites (sp^2-hybridized carbon) on the support that act as anchoring centers for platinum nanoparticles, thus strengthening the nanoparticle-support interaction.[49]

3.3.2. In Situ FTIR Experiments. Figure 9 shows the *in situ* FTIR spectra obtained during CO oxidation on platinum nanoparticles supported on Vulcan XC-72 (Figure 9a) and on MWCNT-m (Figure 9b). The different spectra present two bands which are assigned, respectively, to the stretching of CO linearly bounded to Pt (CO_L) in the 2068−2070 cm^{-1} range and to the CO_2 asymmetric stretching at 2343 cm^{-1}. As stated before, the principal interest of these experiments is the possibility to measure the frequency corresponding to the

dx.doi.org/10.1021/cs4003222 | ACS Catal. 2013, 3, 1940−1950

stretching of the CO molecule adsorbed on the surface of platinum nanoparticles. An eventual shift in this band should here be correlated with the modification of the electron density of platinum nanoparticles resulting from their interaction with the support, as evidenced by XPS and DFT analyses. Indeed, it is well stated that the vibration frequency of CO strongly depends on the electronic properties of the adsorption site: an electronic influence of the support on the catalyst that increases the back-donation of electrons from platinum to the CO antibonding orbitals should increase the CO vibration frequency.[50,51]

In the present study, a shift on the CO band to higher frequencies is observed for Pt/MWCNT-m compared to Pt/Vulcan XC-72. The occurrence of the higher frequency mode of the CO stretching band on the Pt/MWCNT-m catalyst (Δ = 9 cm^{-1}) indicating a weaker bounded state of CO on platinum nanoparticles sites is in good agreement with the XPS results and the CO-stripping curves. Indeed, the above-described support effect changing the energy level of the catalysts and consequently the binding strength of CO_{ads} changes thereby its oxidation potential. The CO_L stretching band position is plotted in Figure 10a as a function of the electrode potential for the two catalysts. It should be noted that a particular band shifts to higher frequencies with the increase of the potential at constant CO_{ad} coverage (Stark shift), and it also shifts in a continuous manner to lower frequencies as the coverage decreases. Indeed, as the number of adsorbed molecules decreases, the competition for the electrons of surface atoms also decreases so that there is more charge available to put into each adsorption site with the consequence that the C−O frequency decreases. The obtained band position shifts can therefore be explained by these two processes. Furthermore, at constant CO_{ad} coverage, before the beginning of the oxidation, the obtained slope (in cm^{-1} V^{-1}) gives us an indication of the CO dipole−dipole interaction.

It was previously shown that the infrared stretching frequency increased with the increase of the particle size, while the Stark Tuning Rate (STR) slope strongly decreased.[52] In this study, the STR slope calculated from in situ FTIR experiments was similar for the two catalysts. This clearly shows that the slight difference in the mean particle size does not affect the CO stripping process. Additionally, it is well-known that the STR slope can be controlled by the number of surface defects.[53] As a conclusion, the first peak observed during CO stripping experiments cannot be related to a higher amount of surface defects responsible for increasing the ability of the catalytic surface to dissociate water and to form OH_{ads} species at defect sites at lower potentials. Thereafter, we can conclude that the difference in the CO_L band frequency obtained is explained by the electronic modification of the platinum nanoparticles.

Integrated CO and CO_2 IR band intensities are plotted in Figure 10b as a function of the electrode potential for the two studied materials. It can been seen that the CO electro-oxidation to CO_2 starts at a lower potential in the Pt/MWCNT-m catalyst as compared with Pt/Vulcan XC-72, while the maximum of the CO_2 band intensity curve occurs at the same potential for the two materials. The negative shift in the oxidation peak potential and the highest C−O stretching frequency obtained for the Pt/MWCNT-m material indicate that the interaction between platinum and the support modifies its electronic properties in a favorable way as to increase the rate of the oxidation of CO as well as tolerance improvement toward carbon monoxide.

4. CONCLUSIONS

Carbon based materials serve as a conductive support for catalytic nanoparticles and may affect their performance in terms of kinetics of charge transfer in electrocatalysis. Owing to its ability to store electrons in the $\pi-\pi$ network of graphitic domains of carbon, the substrate may act as a mediator and stabilizer if coordinating bindings are created between the *d* orbitals of the metal active sites of the nanoparticulated electrocatalysts and the $\pi-\pi$ network. This work provides evidence of a strong interaction between platinum and graphitic domains modifying the electronic properties of platinum nanoparticles as probed by means of CO stripping experiments coupled with *in situ* Fourier transform infrared spectroscopy (FTIR). Changes in the electronic structure of platinum resulting from the interaction of platinum clusters with graphite and its effects on CO adsorption are demonstrated by DFT calculations. The experimental and theoretical results correlate with observations done by XPS. This new interaction feature demonstrates an interesting ingredient that explains the enhanced stability of such platinum nanoparticles on in-plane graphitic domains.

■ ASSOCIATED CONTENT

Ⓢ Supporting Information

Bader charge analysis of Pt atoms, before and after the interaction of Pt38 with the graphite surface. CO adsorption on Pt19 supported on graphite and in the gas phase. TGA curves for Vulcan XC-72 and Pt/Vulcan XC-72 and for MWCNT-m and Pt/MWCNT-m. CO stripping in 0.5 M H_2SO_4 at 25 °C on electrocatalysts for 10 wt % Pt/Vulcan XC-72 and 20 wt % Pt/Vulcan XC-72 synthesized via the carbonyl route. This material is available free of charge via the Internet at http://pubs.acs.org.

■ AUTHOR INFORMATION

Corresponding Author

*E-mail: nicolas.alonso.vante@univ-poitiers.fr (N.A.V.); balbuena@tamu.edu (P.B.B.).

Notes

The authors declare no competing financial interest.

■ ACKNOWLEDGMENTS

J.M. thanks the Ministère de l'Enseignement Supérieur et Recherche (France) for a fellowship and Poitou-Charentes region (France) for financial support. A.L. acknowledges the support from Ministry of Science and Higher Education (Poland) under the grant N N204 527739. We thank Dr. M. Pisarek for XPS measurements. G.R.-S. thanks CONACYT for a postdoctoral fellowship. Computer resources from Texas A&M Supercomputing Center and from Brazos Supercomputing Cluster at Texas A&M University are gratefully acknowledged.

■ REFERENCES

(1) Lewera, A.; Timperman, L.; Roguska, A.; Alonso-Vante, N. *J. Phys. Chem. C* **2011**, *115*, 20153−20159.
(2) Timperman, L.; Feng, Y. J.; Vogel, W.; Alonso-Vante, N. *Electrochim. Acta* **2010**, *55*, 7558−7563.
(3) Ma, J.; Habrioux, A.; Guignard, N.; Alonso-Vante, N. *J. Phys. Chem. C* **2012**, *116*, 21788−21794.

(4) Yang, D. Q.; Zhang, G. X.; Sacher, E.; José-Yacamán, M.; Elizondo, N. *J. Phys. Chem. B* **2006**, *110*, 8348−8356.
(5) Torre, T.; Aricò, A. S.; Alderucci, V.; Antonucci, V.; Giordano, N. *Appl. Catal., A* **1994**, *114*, 257−272.
(6) Ma, J.; Habrioux, A.; Pisarek, M.; Lewera, A.; Alonso-Vante, N. *Electrochem. Commun.* **2013**, *29*, 12−16.
(7) Kondo, T.; Iwasaki, Y.; Honma, Y.; Takagi, Y.; Okada, S.; Nakamura, J. *Phys. Rev. B* **2009**, *80*, 233408.
(8) Oh, J.; Kondo, T.; Hatake, D.; Iwasaki, Y.; Honma, Y.; Suda, Y.; Sekiba, D.; Kudo, H.; Nakamura, J. *J. Phys. Chem. Lett.* **2009**, *1*, 463−466.
(9) Koper, M. T. M.; Lukkien, J. J.; Jansen, A. P. J.; van Santen, R. A. *J. Phys. Chem. B* **1999**, *103*, 5522−5529.
(10) Gasteiger, H. A.; Markovic, N.; Ross, P. N.; Cairns, E. J. *J. Phys. Chem.* **1994**, *98*, 617−625.
(11) Yoo, E.; Okada, T.; Kizuka, T.; Nakamura, J. *J. Power Sources* **2008**, *180*, 221−226.
(12) Coloma, F.; Sepulveda Escribano, A.; Rodriguez Reinoso, F. *J. Catal.* **1995**, *154*, 299−305.
(13) Manzo-Robledo, A.; Boucher, A. C.; Pastor, E.; Alonso-Vante, N. *Fuel Cells* **2002**, *2*, 109−116.
(14) Wang, X.; Waje, M.; Yan, Y. S. *Electrochem. Solid-State Lett.* **2005**, *8*, A42−A44.
(15) Alonso-Vante, N. *Fuel Cells* **2006**, *6*, 182−189.
(16) Longoni, G.; Chini, P. *J. Am. Chem. Soc.* **1976**, *98*, 7225−7231.
(17) Vogel, W. *Cryst. Res. Technol.* **1998**, *33*, 1141−1154.
(18) Schmidt, T. J.; Gasteiger, H. A.; Stab, G. D.; Urban, P. M.; Kolb, D. M.; Behm, R. J. *J. Electrochem. Soc.* **1998**, *145*, 2354−2358.
(19) Ramos-Sanchez, G.; Balbuena, P. B. *Phys. Chem. Chem. Phys.* **2013**, *15*, 11950−11959.
(20) Hu, C. H.; Chizallet, C.; Toulhoat, H.; Raybaud, P. *Phys. Rev. B* **2009**, *79*, 195416.
(21) Lim, D.-H.; Wilcox, J. *J. Phys. Chem. C* **2011**, *115*, 22742−22747.
(22) Lim, D.-H.; Wilcox, J. *J. Phys. Chem. C* **2012**, *116*, 3653−3660.
(23) Grimme, S. *J. Comput. Chem.* **2006**, *27*, 1787−1799.
(24) Bucko, T.; Hafner, J.; Lebègue, S.; Ángyán, J. G. *J. Phys. Chem. A* **2010**, *114*, 11814−11824.
(25) Sławińska, J.; Dabrowski, P.; Zasada, I. *Phys. Rev. B* **2011**, *83*, 245429.
(26) Aradhya, S. V.; Frei, M.; Hybertsen, M. S.; Venkataraman, L. *Nat. Mater.* **2012**, *11*, 872−876.
(27) Błoński, P.; López, N. *J. Phys. Chem. C* **2012**, *116*, 15484−15492.
(28) Methfessel, M.; Paxton, A. T. *Phys. Rev. B* **1989**, *40*, 3616−3621.
(29) Jawhari, T.; Roid, A.; Casado, J. *Carbon* **1995**, *33*, 1561−1565.
(30) Antunes, E. F.; Lobo, A. O.; Corat, E. J.; Trava-Airoldi, V. J.; Martin, A. A.; Veríssimo, C. *Carbon* **2006**, *44*, 2202−2211.
(31) Castillejos, E.; Bachiller-Baeza, B.; Pérez-Cadenas, M.; Gallegos-Suarez, E.; Rodríguez-Ramos, I.; Guerrero-Ruiz, A.; Tamargo-Martinez, K.; Martinez-Alonso, A.; Tascón, J. M. D. *J. Alloy. Compd.* **2012**, *536* (Supplement 1), S460−S463.
(32) Mennella, V.; Monaco, G.; Colangeli, L.; Bussoletti, E. *Carbon* **1995**, *33*, 115−121.
(33) Tang, X. M.; Weber, J.; Mikhailov, S. N.; Müller, C.; Hänni, W.; Hintermann, H. E. *J. Non-Cryst. Solids* **1995**, *185*, 145−150.
(34) Cuesta, A.; Dhamelincourt, P.; Laureyns, J.; Martínez-Alonso, A.; Tascón, J. M. D. *Carbon* **1994**, *32*, 1523−1532.
(35) Vidano, R.; Fischbach, D. B. *J. Am. Ceram. Soc.* **1978**, *61*, 13−17.
(36) Cancado, L. G.; Takai, K.; Enoki, T.; Endo, M.; Kim, Y. A.; Mizusaki, H.; Jorio, A.; Coelho, L. N.; Magalhaes-Paniago, R.; Pimenta, M. A. *Appl. Phys. Lett.* **2006**, *88*, 163106.
(37) Galeano, C.; Meier, J. C.; Peinecke, V.; Bongard, H.; Katsounaros, I.; Topalov, A. A.; Lu, A.; Mayrhofer, K. J. J.; Schüth, F. *J. Am. Chem. Soc.* **2012**, *134*, 20457−20465.
(38) Henkelman, G.; Arnaldsson, A.; Jónsson, H. *Comput. Mater. Sci.* **2006**, *36*, 354−360.
(39) He, D.; Cheng, K.; Li, H.; Peng, T.; Xu, F.; Mu, S.; Pan, M. *Langmuir* **2012**, *28*, 3979−3986.
(40) López-Cudero, A.; Solla-Gullón, J.; Herrero, E.; Aldaz, A.; Feliu, J. M. *J. Electroanal. Chem.* **2010**, *644*, 117−126.
(41) Maillard, F.; Savinova, E. R.; Stimming, U. *J. Electroanal. Chem.* **2007**, *599*, 221−232.
(42) Maillard, F.; Schreier, S.; Hanzlik, M.; Savinova, E. R.; Weinkauf, S.; Stimming, U. *Phys. Chem. Chem. Phys.* **2005**, *7*, 385−393.
(43) Arenz, M.; Mayrhofer, K. J. J.; Stamenkovic, V.; Blizanac, B. B.; Tomoyuki, T.; Ross, P. N.; Markovic, N. M. *J. Am. Chem. Soc.* **2005**, *127*, 6819−6829.
(44) Blyholder, G. *J. Phys. Chem.* **1964**, *68*, 2772−2777.
(45) Bagus, P. S.; Pacchioni, G. *Surf. Sci.* **1992**, *278*, 427−436.
(46) Dimakis, N.; Cowan, M.; Hanson, G.; Smotkin, E. S. *J. Phys. Chem. C* **2009**, *113*, 18730−18739.
(47) Dimakis, N.; Iddir, H.; Díaz-Morales, R. R.; Liu, R.; Bunker, G.; Chung, E.-H.; Smotkin, E. S. *J. Phys. Chem. B* **2005**, *109*, 1839−1848.
(48) Fang, H.-T.; Liu, C.-G.; Liu, C.; Li, F.; Liu, M.; Cheng, H.-M. *Chem. Mater.* **2004**, *16*, 5744−5750.
(49) Coloma, F.; Sepulveda-Escribano, A.; Fierro, J. L. G.; Rodriguez-Reinoso, F. *Langmuir* **1994**, *10*, 750−755.
(50) Savinova, E. R.; Hahn, F.; Alonso-Vante, N. *Surf. Sci.* **2009**, *603*, 1892−1899.
(51) Ruiz Camacho, B.; Morais, C.; Valenzuela, M. A.; Alonso-Vante, N. *Catal. Today* **2013**, *202*, 36−43.
(52) Rice, C.; Tong, Y.; Oldfield, E.; Wieckowski, A.; Hahn, F.; Gloaguen, F.; Léger, J.-M.; Lamy, C. *J. Phys. Chem. B* **2000**, *104*, 5803−5807.
(53) Stamenkovic, V.; Chou, K. C.; Somorjai, G. A.; Ross, P. N.; Markovic, N. M. *J. Phys. Chem. B* **2004**, *109*, 678−680.